Polymer Chemistry

Transformation of Semicrystalline Polymer Mechanics by Cyclic Polymers

Journal:	*Polymer Chemistry*
Manuscript ID	PY-ART-11-2024-001269.R2
Article Type:	Paper
Date Submitted by the Author:	17-Dec-2024

Complete List of Authors:	Bension, Yishayah; University of South Carolina Columbia, Department of Chemistry and Biochemistry Wijesekera, Andrew; University of South Carolina Columbia, Department of Chemistry and Biochemistry Collins, Coby; University of South Carolina Columbia, Department of Chemistry and Biochemistry Zheng, Juncheng; Michigan State University, Department of Chemical Engineering and Materials Science Zhao, Hai; University of South Carolina Columbia, Department of Chemistry and Biochemistry Ge, Ting; University of South Carolina Columbia, Department of Chemistry and Biochemistry Tang, Chuanbing; University of South Carolina Columbia, Department of Chemistry and Biochemistry Zhang, Siteng; University of South Carolina, Chemistry and Biochemistry Cheng, Shiwang; Michigan State University, Chemical Engineering and Materials Science Stefik, Morgan; University of South Carolina, Chemistry and Biochemistry; University of South Carolina Columbia, Department of Chemistry and Biochemistry

Transformation of Semicrystalline Polymer Mechanics by Cyclic Polymers

Yishayah Bension,[1] Andrew Wijesekera,[1] Coby S. Collins,[1] Siteng Zhang,[1] Juncheng Zheng,[2] Hai Zhao,[1] Shiwang Cheng,[2] Morgan Stefik,[1] Ting Ge,[1,*] and Chuanbing Tang[1,*]

[1] Department of Chemistry and Biochemistry, University of South Carolina, Columbia, South Carolina 29208, United States

[2] Department of Chemical Engineering and Materials Science, Michigan State University, East Lansing, Michigan 48824, United States

Corresponding Author Email: tingg@mailbox.sc.edu (T.G.); tang4@mailbox.sc.edu (C.T.)

Abstract

Cyclic polymers, lacking chain ends and featuring unique topological constraints, offer distinctive mechanical and thermal behaviors. This study synthesizes and compares semicrystalline linear and cyclic polycyclooctene (PCOE), with linear PCOE produced via ring-opening metathesis polymerization (ROMP) and cyclic PCOE via ring-expansion metathesis polymerization (REMP). Mechanical, thermal, and crystalline properties were evaluated through tensile testing, dynamic mechanical analysis (DMA), and wide-angle X-ray scattering (WAXS). Findings reveal that crosslinked cyclic PCOE exhibits lower tensile strength but greater stretchability than its linear counterpart, indicating enhanced network softness. DMA results show cyclic PCOE has a lower glass transition temperature T_g and rubbery plateau modulus $G'_{rubbery}$, while WAXS indicates lower crystallinity in cyclic PCOE < 25%, stabilizing at approximately 15% under a tensile strain of 100%. These differences suggest that polymer topology, not crystallinity, primarily dictates the mechanical response. Molecular dynamics simulations, using a crystallizable model of polyethylene, replicate the lower stress and higher stretchability observed experimentally, highlighting more compact cyclic polymer conformations with fewer entanglements. The results align with past studies on amorphous cyclic polymers, providing deeper insights into how cyclic structures affect semicrystalline polymer mechanics. This combined experimental and simulation approach advances understanding of cyclic polymer architectures and their transformative impact on polymer properties.

Introduction

Polymer architectures play an important role in dictating the physical properties of materials.[1-9] The research on the role of polymer architectures has focused on conventional linear polymers due to their dominance in commercial products, facile synthesis, and cheap production. As one example, it has been demonstrated that branching or crosslinking linear polymers can greatly impact the material properties. Going beyond linear polymers, nonlinear architectures may be synthesized and characterized because of the advances in polymer chemistry. This has generated extensive research interest in transforming material properties by nonlinear polymer architectures.

Cyclic polymers lie at the frontier of research on nonlinear polymer architectures.[10-22] This is driven partly by the progress in synthesizing high-molecular-weight cyclic polymers. One straightforward strategy for synthesizing cyclic polymers is to first synthesize the linear chain and then couple the two chain ends together.[23-31] This strategy via a bimolecular or an unimolecular ring closure is difficult to scale up due to an inherent disadvantage from the competition between oligomerization and cyclization. Cyclization may outcompete oligomerization in a dilute solution, which requires a large amount of solvents to reach a very low polymer concentration. However, both the yields and the molecular weights of cyclic polymers synthesized in this way are low, making it difficult to study macroscopic material properties. A powerful alternative strategy to synthesize cyclic polymers is ring expansion.[32-38] Developed by Grubbs et al. in 2002, ring expansion metathesis polymerization (REMP) uses metathesis to insert monomers into existing cyclic olefins. The starting monomer possesses a ring structure, and therefore, no cyclization of two chain ends is needed. As such, REMP overcomes the entropic penalty of molecular ring closure and the limitation on molecular weight. This strategy enables the synthesis of cyclic polymers with high yields and high molecular weights (> 100 kDa) and is favored in the research on the material properties of cyclic polymers.

Another motivation for exploring the use of cyclic polymers as transformative components of materials is their unique conformations and dynamics. Cyclic polymers at high concentrations impose the topological constraints of non-concatenation on each other. As a result, cyclic polymers are in globular conformations that are more compact than the random-walk conformations of linear polymers.[39, 40] The mutual overlap of globular cyclic polymers is limited, resulting in fewer polymer entanglements per polymer chain. Accordingly, cyclic polymers in melts and

concentrated solutions move faster than linear polymers, as manifested in the faster stress relaxation and lower viscosity.[39, 41] Moreover, for crystallizable polymers, the faster dynamics of cyclic polymers facilitate the kinetics of crystallization upon cooling.[17, 42]

The mechanics of cyclic polymers in solid states have been investigated recently by large-scale molecular simulations using the generic coarse-grained bead-spring model.[15,19] The mechanical properties are important as they provide an essential foundation for many functions of polymeric materials. The simulations of cyclic polymers in the glassy state showed that craze fibrils, which precede cracks in mechanical failure, may form steadily for sufficiently high molecular weights.[19] Compared with crazing in glassy linear polymers, the craze fibrils in glassy cyclic polymers are of lower density, and the drawing stress for crazing is reduced. These changes are caused by the reduction of entanglement density in the glassy cyclic polymers. The simulations of crosslinked cyclic polymers as elastomers showed that the network shear modulus is lower than that of crosslinked linear polymers, and the maximum extension before failure is larger.[15] The enhanced network softness and stretchability arise from the lower density of entanglements trapped between crosslinks. In addition to the simulations, theories for linear polymer mechanics have been extended to describe cyclic polymer mechanics.[15,19] Although computational and theoretical studies have demonstrated the capability of cyclic polymers in transforming polymer mechanics, extensive experiments have yet to be performed to evaluate the mechanics of cyclic polymers.

Herein, we report the synthesis of linear and cyclic polycyclooctene (PCOE) and compare their mechanical properties at various concentrations of crosslinks. Since the crosslinked PCOE samples are semicrystalline, we measure their crystallinity before and after tensile strain. Besides experiments, we perform molecular dynamics simulations using a coarse-grained model of polyethylene to examine the microscopic details regarding how cyclic architecture affects semicrystalline polymer mechanics. The differing network topology of crosslinked semicrystalline linear and cyclic polymers, as revealed by the simulations, are shown in **Figure 1**. The joint experiment and simulation work elucidates the role of cyclic architecture in semicrystalline polymer mechanics.

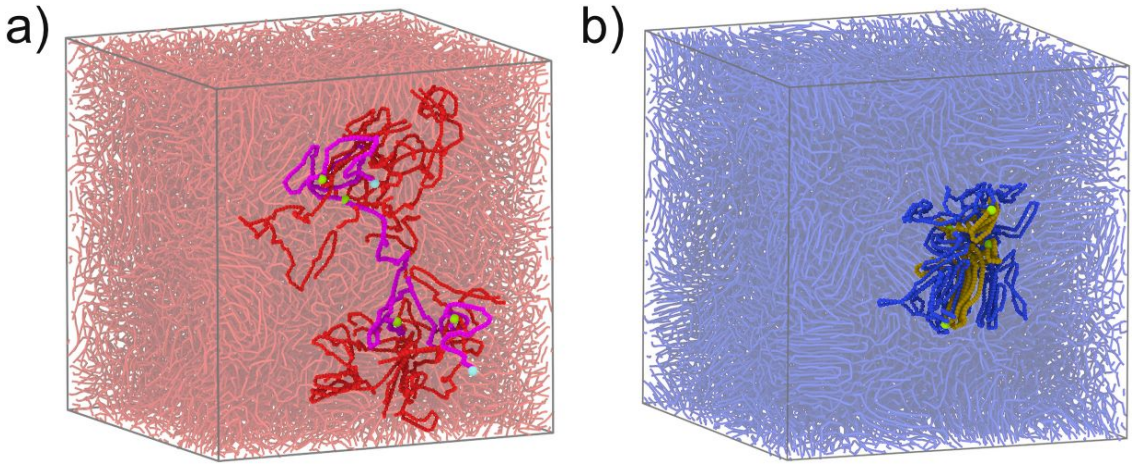

Figure 1. Network topology of crosslinked semicrystalline polymers, as revealed by the simulations: a) a linear polymer (magenta with chain ends in cyan) crosslinked with nearby linear polymers (red) in a network (dimmed red); b) a cyclic polymer (dark yellow) crosslinked with nearby cyclic polymers (blue) in a network (dimmed blue). Crosslinks are highlighted in green.

Experiments

Materials

Phosphoric acid (85%, Fisher chemical), ammonium chloride (98%, Fisher chemical), paraformaldehyde (Sigma-Aldrich), glyoxal (40% w/w, Thermo Scientific), cis-Cyclooctene (95%, Thermo Scientific), 6-Bromo-1-hexene (95.0%, TCI America), potassium tert-butoxide (98%, Thermo Scientific), and dicumyl peroxide (DCP) (98%, Sigma-Aldrich) were used as is. Grubbs catalysts M102 and M204 were purchased from Sigma-Aldrich and stored in the glovebox. All solvents, including methanol (MeOH), dichloromethane (DCM), tetrahydrofuran (THF), and toluene, were dried over alumina prior to use. All other reagents were from commercial resources and used as received.

Ring-expansion Metathesis Polymerization of cis-Cyclooctene

In a glovebox, cis-cyclooctene was weighed (3.0 g, 27.2 mmol) into a 40 mL dram vial equipped with a stir bar. 35 mL toluene was added and then REMP catalyst (1.2 mg, 8.3×10^{-4} mmol) was added as a solution in 1 mL toluene, and the reaction mixture was heated to 40 °C overnight using an aluminum heat block. The polymer was then precipitated in cold methanol outside the glovebox. The resulting white polymer was then redissolved in hot THF and precipitated in cold methanol

twice. The polymer (cyclic polycyclooctene, C-PCOE) was stored under vacuum in the dark at room temperature.

Ring-opening Metathesis Polymerization of cis-Cyclooctene

In a glovebox, cis-cyclooctene was weighed (3.0 g, 27.2 mmol) into a 40 mL dram vial equipped with a stir bar. 30 mL DCM was added and then G-2 catalyst (0.2 mg, 2.4×10^{-4} mmol) was added as a solution in 1 mL DCM and the reaction mixture was left to stir at room temperature overnight. The polymer was precipitated in cold methanol outside the glovebox. The resulting white polymer was then redissolved in hot THF and precipitated in cold methanol twice. The polymer (linear polycyclooctene, L-PCOE) was stored under vacuum in the dark at room temperature.

Synthesis of Crosslinked Polycyclooctene

In an Erlenmeyer flask, 3 g of PCOE was dissolved in 50 mL THF at 30 °C. Then 30 mg of DCP was added, the reaction mixture was poured into a Teflon mold, and the solvent was allowed to evaporate under vacuum. The dried films were then cut into small square pieces (1 mm^2) and placed in the hot press with a 58 cm^2 square mold at a temperature of 150 °C under 7 metric tons of pressure. The polymer was cured for 20 minutes and then removed from the hot press and allowed to cool to room temperature. The crosslinked film was allowed to cure further under vacuum overnight. The film was then cut into the required shape for testing.

Nuclear Magnetic Resonance Spectroscopy (NMR)

NMR spectra were recorded on a Bruker Avance III (400 or 300 MHz). Chemical shifts were reported in ppm with TMS as an internal standard (TMS 0.00 ppm for ^1H and ^{13}C, DMSO δ 2.5 ppm and 39.52 for ^1H and ^{13}C, respectively, $CDCl_3$ δ 7.26 ppm and 77.2 for ^1H and ^{13}C, respectively).

Differential Scanning Calorimetry (DSC)

A differential scanning calorimeter (Hitachi 7020) was used to analyze the thermal properties of the thermosets. A sample (5–10 mg) was encapsulated in a 40 μL aluminum pan. The sample was submitted (I) heating from 25 to 150 °C, (II) cooling to −60 °C, and (III) heating to 150 °C with cooling and heating rates at 10 °C/min under a nitrogen atmosphere.

Thermogravimetric Analysis (TGA)

Thermogravimetric analysis (Hitachi 7200) was used to analyze the thermal properties of the thermosets. A sample (10–15 mg) was encapsulated in a 60 μL Pt pan. The sample was then heated to 800 °C with a heating rate of 10 °C/min under a nitrogen atmosphere.

Size Exclusion Chromatography (SEC)

Samples were run on a Tosoh EcoSEC Elite Model HLC-8420 with the integrated RID, $LENS_3$/VISC detector connected in parallel. Samples were injected at 100 µL at 40 °C in THF with a flow rate of 1 mL/min on two TSKgel (5 µm, 7.8 nm, ID x 30 cm). The system was calibrated universally using polystyrene standards.

Tensile Experiments

Tensile stress-strain testing was conducted on an Instron 5543A testing instrument. Thermoset samples were prepared with a cross-sectional length of 20 mm and a width of 5.0 mm. The thickness was between 0.45 and 0.51 mm. Tests were done at room temperature with a crosshead speed of 5 mm/min.

Dynamic Mechanical Analysis (DMA)

Dynamic mechanical analysis was carried out on the polymer samples in DMA 850 (TA Instruments) operating in the tension mode oscillation-temperature ramp from -150 to 100 °C at a frequency of 1 Hz upon heating. The amplitude was 5 µm with a pre-load force of 0.1 N. The heating rate was set to be 5 °C min^{-1}. Liquid nitrogen was used to achieve the sub-ambient temperature. The molecular weight between effective crosslinks was calculated as

$$M_c = 3RT\rho/G'_{Rubbery} \qquad (1)$$

where R is the universal gas constant, T is the temperature, ρ is the polymer's density, and $G'_{Rubbery}$ refers to the rubbery plateau of the storage modulus.

Wide-Angle X-ray Scattering (WAXS)

WAXS measurements were performed at the South Carolina SAXS Collaborative (SCSC) using a SAXSLab Ganesha instrument. A Xenocs GeniX3D microfocus source was used with a Cu target to create a monochromatic beam with a wavelength of 0.154 nm. The instrument was calibrated with NIST reference material 640d silicon powder, with reference peak position of $2\theta = 28.44°$, where 2θ is the total scattering angle. A Pilatus 300K detector (Dectris) was used to collect the 2D scattering patterns. The detector exhibits nominal pixel dimensions of 172 × 172 μm^2. The WAXS data was acquired with an x-ray intensity of $\approx$ 36.3 million photons s^{-1} upon the sample. The sample-to-detector distance was 112.1 mm. The 2D images were azimuthally integrated to yield scattering vector or azimuthal angle and intensity using SAXSGUI software. The percent crystallinity and orientational order parameter were determined using custom Matlab scripts.

Results and Discussion

Synthesis of Cyclic and Linear Polycyclooctene

Both linear and cyclic polymers were respectively synthesized using ring-opening metathesis polymerization (ROMP) and ring expansion metathesis polymerization (REMP) (**Figure 2a**). Grubbs 2nd generation catalyst was used for ROMP toward linear polymers. Since the REMP catalyst is not commercially available, it was synthesized in this work (see Supporting Information). By controlling the molar ratio of cyclooctene to catalyst, both polymerization techniques led to PCOE with high molecular weight.

Additionally, in order to verify the synthesis of PCOE with a cyclic topology, C-PCOE was further functionalized with methyl 3-mercaptopropionate (Mmp) (**Figure 2b**) via thiol-ene click chemistry, yielding branched PCOE (Mmp-PCOE). The synthesis of Mmp-PCOE was verified using ^{1}H NMR spectroscopy. From the stacked spectra (**Figure 2c**), the chemical shift at δ = 5.2 ppm, which corresponds to the alkene protons, disappeared. Furthermore, the appearance of peaks at δ = 2.8 and 3.8 ppm was attributed to protons adjacent to the ester group. The transformation was also observed by the physical change in the polymer from being ductile to viscous. This was further supported by the DSC curve, which shows the absence of a melting peak (70 °C) seen in the original material (**Figure S11**) in the new polymer due to the presence of side groups that disrupt the crystallization of polymers (**Figure 2d**).

The direct verification of a cyclic topology was supported by AFM imaging **(Figure 3a)**. Under dilute conditions, the modified cyclic polymer chains (**Figure 2b**) were spin-coated onto a mica substrate and shown to possess a cyclic architecture. Surface height analysis performed by AFM showed the diameter of these polymers to be approximately 50-60 nm **(Figure 3b)**. The AFM imaging suggested that any contamination from concatenated or linear chains would be minimal. Furthermore, triple detection of the cyclic polymers by SEC analysis **(Figure 3c-e)** matches previously reported data in the literature.[36]

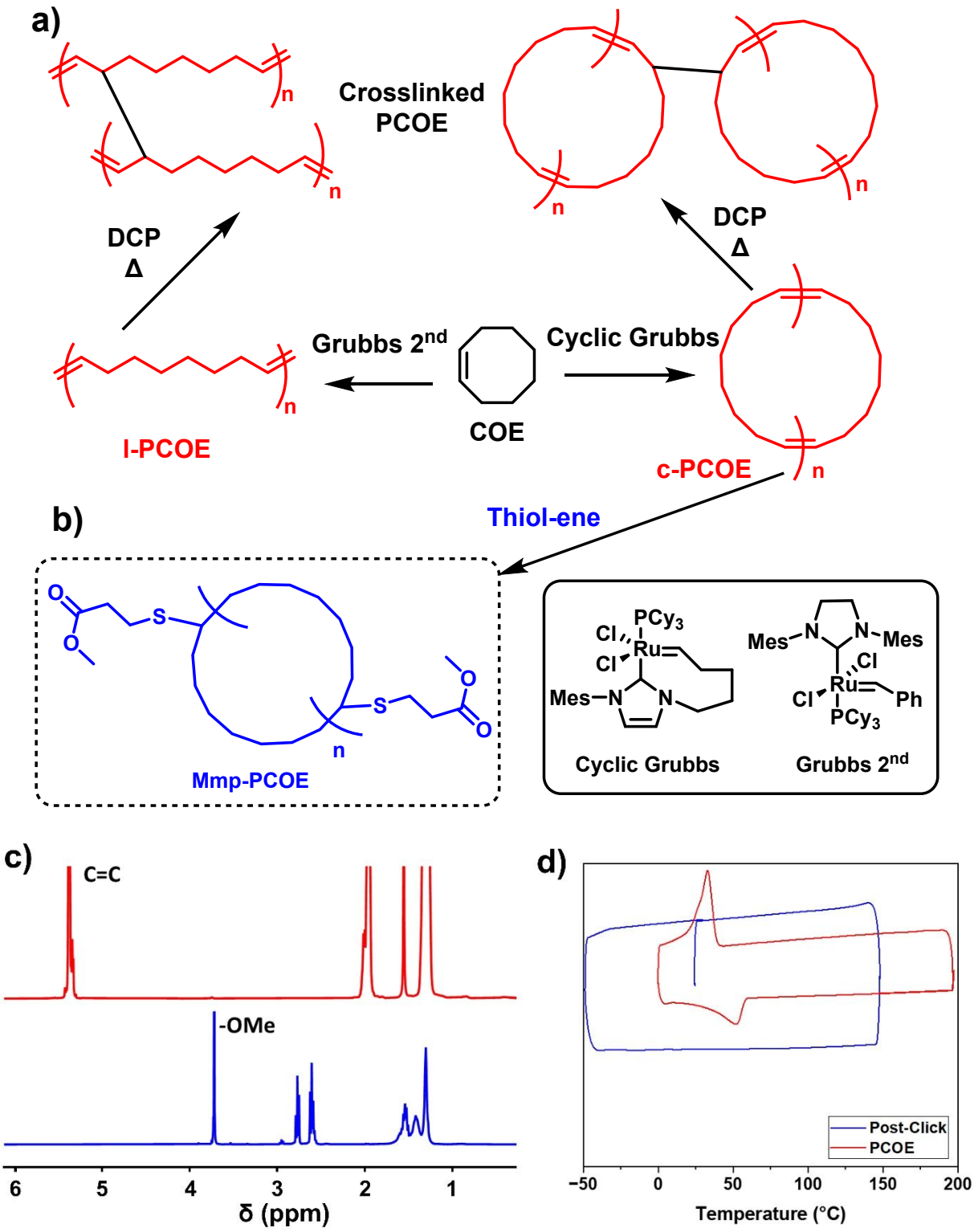

Figure 2. a) Synthesis of crosslinked linear and cyclic PCOE; **b**) preparation of cyclic PCOE grafted with methylmercaptopropanoate (Mmp-PCOE); **c**) stacked ^{1}H NMR spectra and **d**) DSC curves of cyclic PCOE and Mmp-PCOE (see supporting information for experimental details).

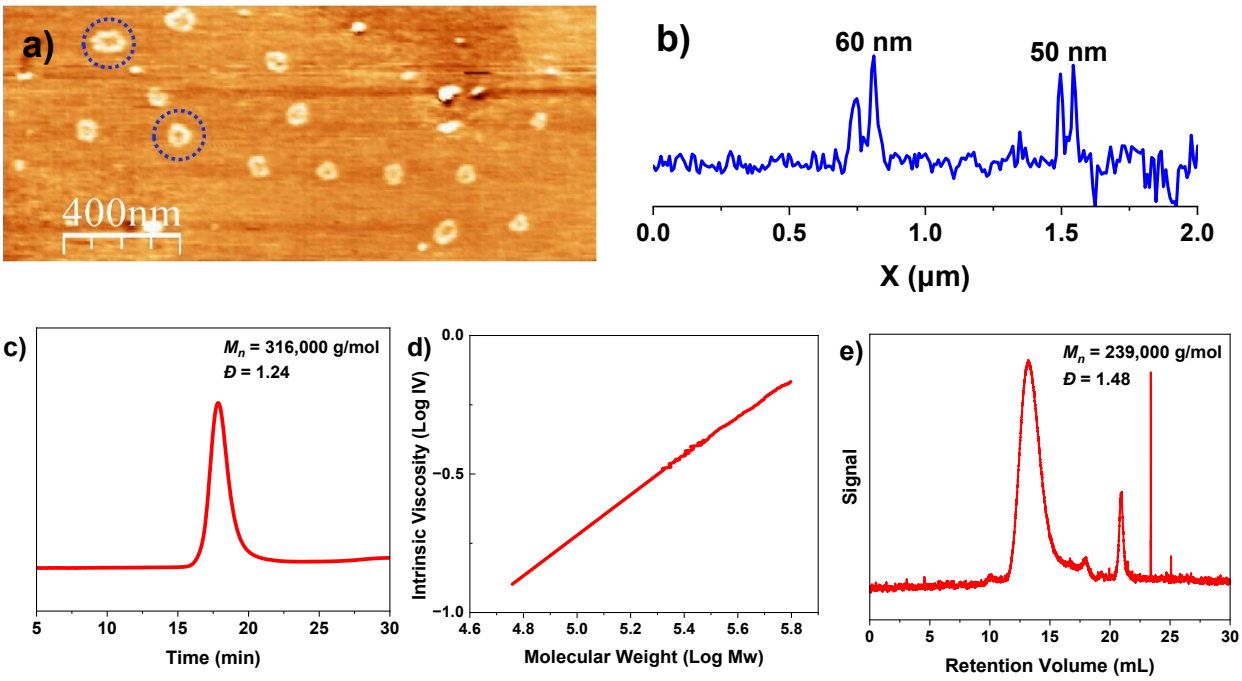

Figure 3. Analysis of cyclic Mmp-PCOE; a) atomic force microscopy (height image) with two cyclic polymers highlighted by blue dashed circles; (b) cross-sectional plot from the AFM height image; c) SEC refractive index signal; d) SEC viscosity; and (e) SEC multi-angle light scattering.

Mechanical Properties of Crosslinked Polycyclooctene

Once the cyclic architecture was confirmed, the tensile properties of linear and cyclic polymers were explored. Virgin PCOE is difficult to process for mechanical testing due to their inability to form free-standing films, so DCP was added to crosslink the materials, as illustrated in **Figure 2a**. 0.75, 1.0, and 1.5 wt% of DCP were chosen (**Figure S9**). The results from the tensile experiments are summarized in **Figure 4** and **Table 1.** The tensile stress at break peaks with 1.0 wt% DCP, and further increase of DCP led to reduced stress (**Figure 4d**). Meanwhile, an increase in DCP wt% led to reduced tensile strain at break (**Figure 4e**).

The mechanical properties of the crosslinked cyclic and linear polymers are different. First, the tensile stress at break is consistently lower for the cyclic polymers. This can be most easily observed at 1.0 wt.% DCP (**Figure 4b**), where the tensile stress at break for the cyclic polymer is 0.86 MPa lower than that for the linear polymer. Second, the cyclic polymers exhibit higher stretchability than the corresponding linear polymers, by up to 137% when the 1.5 wt% DCP was used (**Figure 4c**). In short, at the same crosslinking density, the crosslinked cyclic PCOE exhibits

lower tensile strength than the crosslinked linear PCOE but may be stretched to a larger strain before failure. These trends are consistent with previous simulation results for amorphous cyclic polymer mechanics, reflecting few entanglements trapped in the crosslinked cyclic polymers.[15,19]

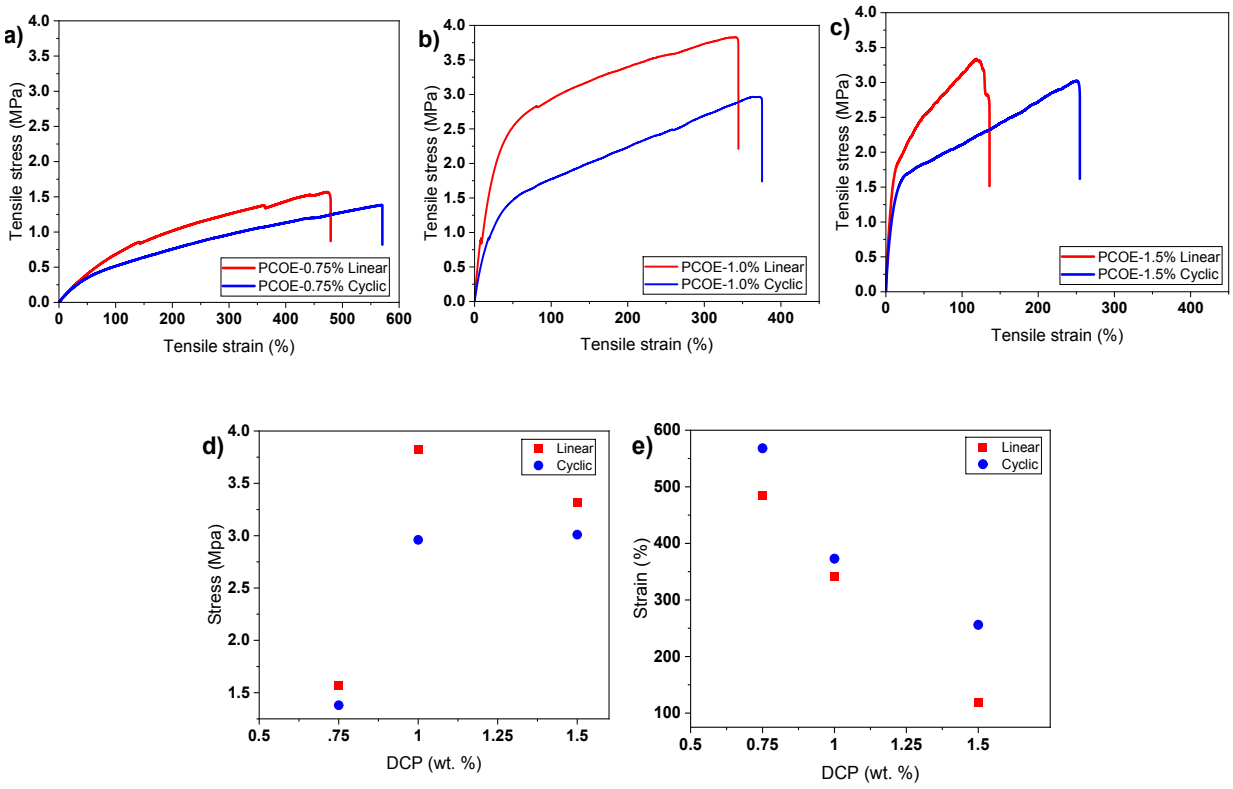

Figure 4. Tensile test results for cyclic and linear PCOE with different DCP wt%: a) 0.75%; b) 1.0 %; c) 1.5%; d) the stress at break as a function of DCP wt%; e) the strain at break as a function of DCP wt%.

Table 1. Tensile properties of crosslinked linear and cyclic PCOE

	Linear PCOE (M_n = 220 kDa)			Cyclic PCOE (M_n = 239 kDa)		
DCP (wt%)	0.75%	1.0%	1.5%	0.75%	1.0%	1.5%
Stress at break (MPa)	1.57	3.82	3.32	1.38	2.96	3.01
Strain at break (%)	475	341	119	568	373	256

Dynamic Mechanical Analysis

Figure 5a and **Figure 5b** show the storage (G′) and loss (G″) moduli as functions of temperature. All samples exhibit the transition from the glassy state to the rubbery plateau as the temperature increases. The values of the glass transition temperature T_g, which corresponds to the peak of tanδ in **Figure 5c**, are listed in **Table 2**. There is a minor increase in T_g as the crosslinking density increases for both linear and cyclic PCOE. T_g of the cyclic PCOE is noticeably lower than that of the linear PCOE by about 15 °C at the same crosslinking density. The experiments employed may not reveal sufficient insights about the effects of the cyclic polymer topology on the glass transition in amorphous polymers. Due to crystallinity, one cannot draw conclusions about the effects of cyclic polymer topology on the glass transition temperature of amorphous polymers from the limited experimental data obtained in this work. The role of polymer topology in the glass transition of amorphous polymers could be an important topic for future research.

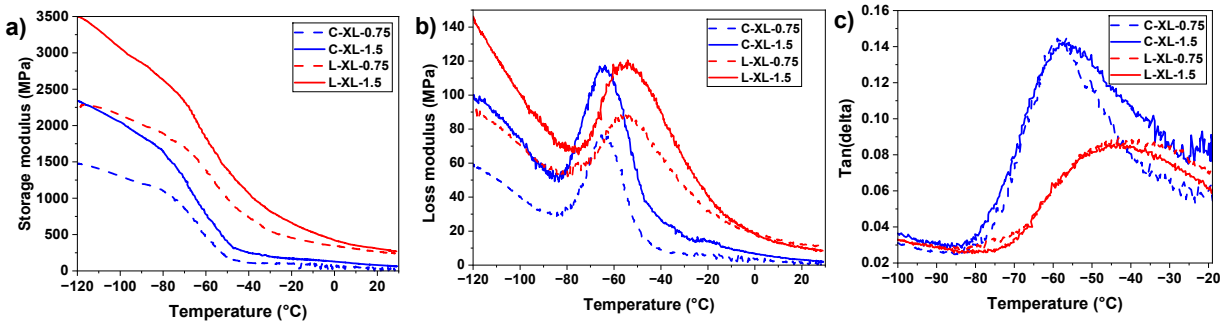

Figure 5. DMA results for the crosslinked linear and cyclic PCOE: (a) Storage modulus (G′); (b) loss modulus (G″); (c) tanδ.

The rubbery plateau $G'_{Rubbery}$ of the storage modulus increases with the crosslinking density, as there are more stress-carrying network strands within the same volume upon deformation. $G'_{Rubbery}$ of the cyclic PCOE is lower than that of the linear PCOE at the same crosslinking density. Using Eq. (1) in the Experimental part, the molecular weight M_c between effective crosslinks, which includes both the chemical crosslinks and the physical entanglements trapped in the crosslinked network, is computed based on $G'_{Rubbery}$. The values of M_c are listed in **Table 2**. Cyclic PCOE with lower $G'_{Rubbery}$ has a larger M_c, indicating fewer physical entanglements per strand between the chemical crosslinks.

Table 2. T_g and M_c from DMA of the crosslinked samples.

Sample	T_g (°C)	M_c (Da)
C-XL-0.75	-59	2599
C-XL-1.5	-58	2429
L-XL-0.75	-45	778
L-XL-1.5	-44	606

Crystallinity of Crosslinked Polycyclooctene

Based on the DSC result (**Figure S11**), it is evident that the synthesized PCOE samples were semicrystalline. Polymer crystallinity was analyzed using WAXS measurements. **Figure 6** shows the WAXS patterns for linear and cyclic polymers, both before and after the deformation to a tensile strain of 100%, and with variable DCP loading. The broad amorphous hump (gray) and crystalline peaks were integrated and compared to determine the percent crystallinity (crystalline intensity/total intensity), as summarized in **Table 3**. The crystallinity varied with polymer architecture. The as-made linear polymers (~22%) were generally more crystalline than cyclic analogs (~13%). Curiously, the percent crystallinity for all samples converged to ~15% after a tensile strain of 100%, slightly decreasing the crystallinity for linear chains and slightly increasing the crystallinity for cyclic chains. Strain-induced disruption of misaligned crystals and strain-induced crystal formation aligned with the strain direction can both contribute to the changes in percent crystallinity. Unlike polymer architecture, the DCP loading in the investigated range had surprisingly minor effects on the crystallinity.

Table 3. Percent crystallinity and orientation order parameter (S) of crosslinked polymers

Sample	Crystallinity (%) Before Deformation	Crystallinity (%) After Deformation	S, Orientation Order After Deformation
l-XL-0.75	23.5	15.4	0.91
l-XL-1.5	20.8	15.1	0.88
c-XL-0.75	12.0	15.3	0.81
c-XL-1.5	13.8	15.1	0.85

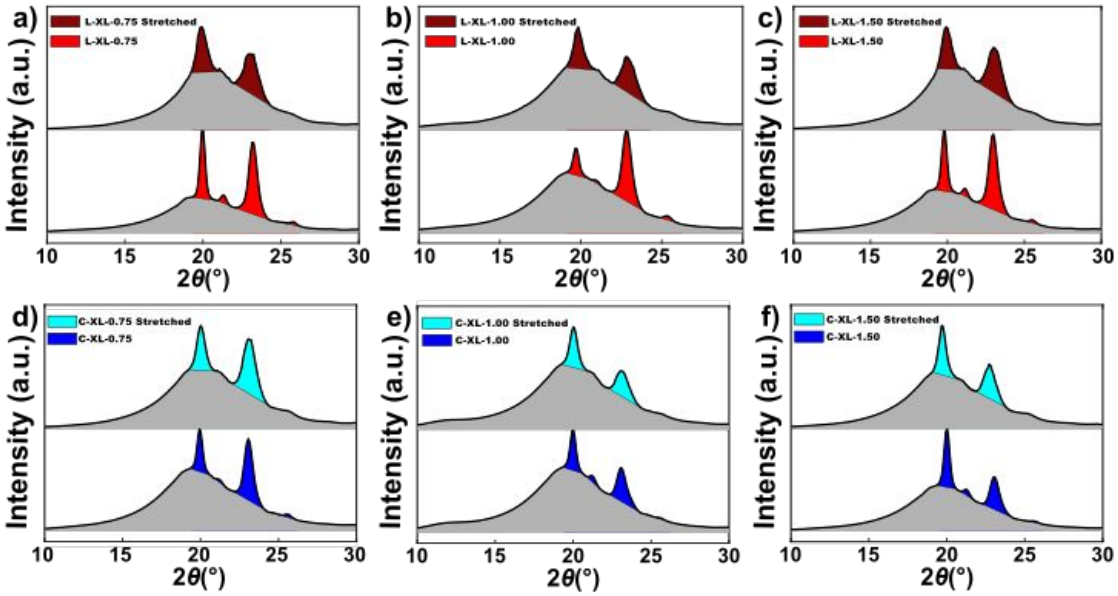

Figure 6. WAXS profiles of crosslinked linear (top row) and cyclic (bottom row) polycyclooctene with DCP at: a/d) 0.75 wt%; b/e) 1.0 wt%; c/f) 1.5 wt%. The gray-shaded areas correspond to the amorphous content, and the other shaded areas correspond to the integrated crystalline content.

The WAXS data showed strain-induced formation of orientated crystallites, as expected for elastomeric rubbers (**Figure 7**). This orientation is apparent in the 2D data where the crystalline diffraction from as-made samples is non-oriented with isotropic rings (**Figure 7a**) and then transforms with strain into azimuthally-localized intensity profiles (**Figure 7b**). The scattered intensity was extracted as a function of the azimuthal angle for the (110) peak ($0.134 < q < 0.146$ nm^{-1}, ± 3 standard deviations). The resulting azimuthal profiles from as-made samples show the

constant diffracted intensity as expected for non-oriented crystals. In contrast, the stretched samples each exhibited two localized zones of enhanced intensity (180° apart) corresponding to the new crystallites formed during uniaxial strain. The extent of ordering was quantified by calculating orientation order parameters *S* using:

$$S = \frac{3}{2}\frac{\int_0^{\pi} exp\left\{\frac{-\alpha_d^2}{2\sigma^2}\right\}\sin(\alpha_d)\cos^2(\alpha_d)d\alpha_d}{\int_0^{\pi} exp\left\{\frac{-\alpha_d^2}{2\sigma^2}\right\}\sin(\alpha_d)\,d\alpha_d} \quad (2)$$

where α_d is the azimuthal angle relative to the director and σ is the standard deviation (peak width in radians) determined by best-fits to the measured intensity profiles.[43] Here, α_d is zero at the peak of intensity, whereas the instrument coordinate system for azimuthal angle (α) is indicated in **Figure 7**. These data show that the cyclic polymers (S~0.83) are less oriented (broader peaks in azimuthal direction) after stretching as compared to linear analogs (S~0.90), suggestive of fewer rearrangements because of the cyclic polymer architecture. The variation of DCP content had a minor effect on the orientation parameters. The result that the crosslinked PCOE samples have almost the same crystallinity at the same tensile strain, regardless of the polymer chain architecture and crosslink density, rules out crystallinity as the dominant factor controlling the mechanical response.

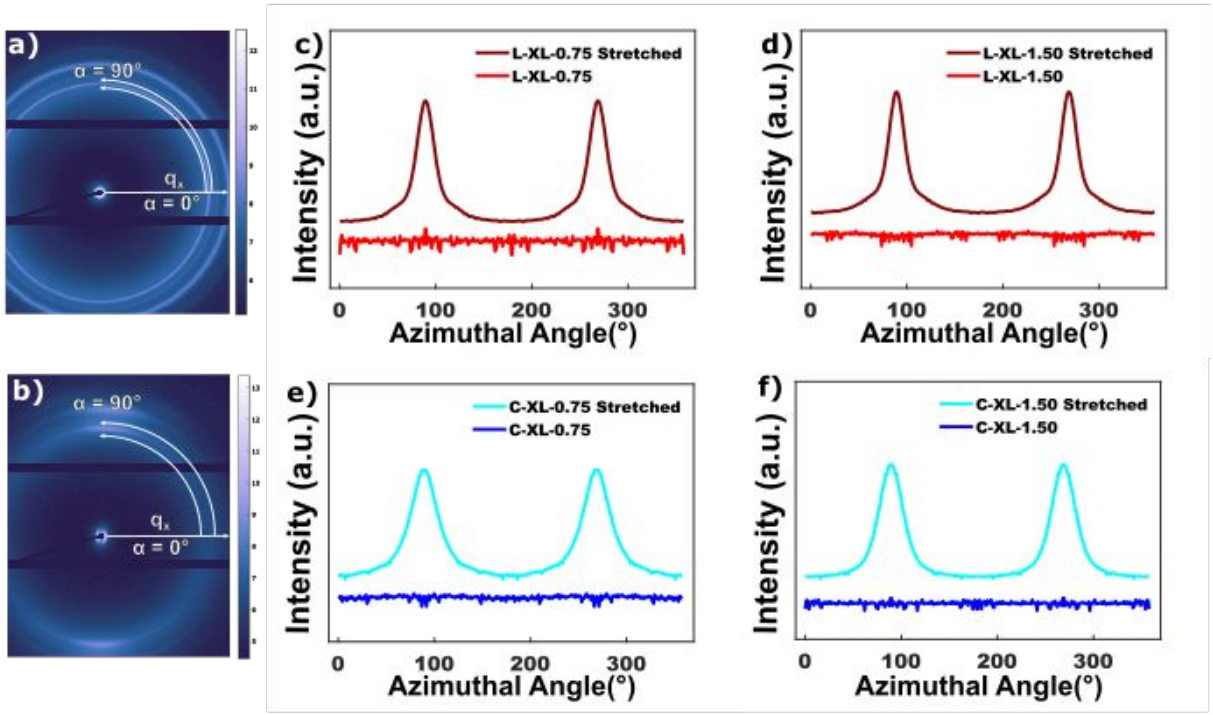

Figure 7. 2D WAXS data from (a) an as-made sample with isotropic diffraction and (b) a strained sample with preferred crystallite orientations. Azimuthal intensity profiles were extracted (see white bounding lines in a/b) for (c,d) linear polymers and (e,f) cyclic polymers with various DCP content (indicated in caption).

Molecular Dynamic Simulations

To further understand the microscopic picture underlying the enhanced network softness and stretchability of crosslinked semicrystalline cyclic polymers, we performed molecular dynamics simulations. Compared to the experiments, the unique strengths of simulations are the precise control of the polymer network topology and the access to microscopic details. The coarse-grained (CG) united-monomer model for polyethylene (PE) is used.[44] One CG bead of size σ and mass m represents one ethylene monomer C_2H_4. Adjacent CG beads in a polymer chain are connected by harmonic bonds with equilibrium bond length of $0.5\,\sigma$ and spring constant $k_{bond} = 1350 k_B T_0/\sigma^2$, where $T_0 = 500\,K$ is the reference temperature. A bond-bending angular potential is employed for two neighboring bonds along the polymer chain. The angular potential is tabulated based on the torsional interactions in all-atom PE simulations. All non-bonded interactions, including both inter-molecular interactions and intra-molecular interactions where beads are separated by three or more consecutive bonds, are modeled using the pairwise 9-6 Lennard-Jones (LJ) potentials with interaction strength $\varepsilon_{LJ} = 0.37775\,k_B T_0$, LJ bead size $\sigma_{LJ} = 0.89\sigma$, and cut-off distance $r_c = 1.02\,\sigma$. The simulation unit time is $\tau = \sqrt{m\sigma^2/k_B T_0}$. The mapping from the simulation units to real units is $\sigma = 0.5\ nm$, $m = 27.388\ g/mol$, and $\tau = 2.7\ ps$.

To generate a simulation sample, $M = 200$ polymers, each consisting of $N = 400$ CG beads, were placed in a cubic simulation box with periodic boundary conditions. Two samples were created, one with linear polymers and the other with non-concatenated cyclic polymers. Each sample was first equilibrated in the melt state at constant temperature $T = T_0 = 500\,K$ and constant pressure $P = 8.0 k_B T_0/\sigma^3$. The temperature was controlled using the Langevin thermostat with characteristic damping time $2\,\tau$, while the pressure was controlled using the Berendsen barostat with characteristic damping time $100\,\tau$. The equations of motion were integrated with a time step of $0.01\,\tau$. This equilibration stage ended when the melt density reached $\rho = 2.12\,m/\sigma^3$. Subsequently, the melt sample was further equilibrated at $T = T_0$ using the

Langevin thermostat with characteristic damping time 2 τ. All simulations in this work were conducted using the LAMMPS package.[45]

The equilibration of the melt samples is confirmed by the chain conformation statistics. **Figure 8** shows $C(n) = \langle R^2(n)\rangle / 2nl_{C-C}^2$, where $\langle R^2(n)\rangle$ is the mean square end-to-end distance between a CG bead and its n^{th} neighbor along the chain, and $l_{C-C} = 0.154\ nm = 0.308\ \sigma$ is the length of a C-C bond. For the linear polymer melt, $C(n)$ rises with increasing n and approaches Flory's characteristic ratio $C_\infty = 7.4$ of PE in the limit of large n, indicating the equilibration of the sample.[46] For the cyclic polymer melt, $C(n)$ is computed only for n up to $N/2 = 200$. $C(n)$ at small n overlaps with that for the linear polymers, showing polymer topology does not affect local chain conformations. With increasing n, $C(n)$ for the cyclic polymers deviates from that for the linear polymers, as non-concatenated cyclic polymers adopt the globular conformations that are more compact than random-walk coils.[39, 40]

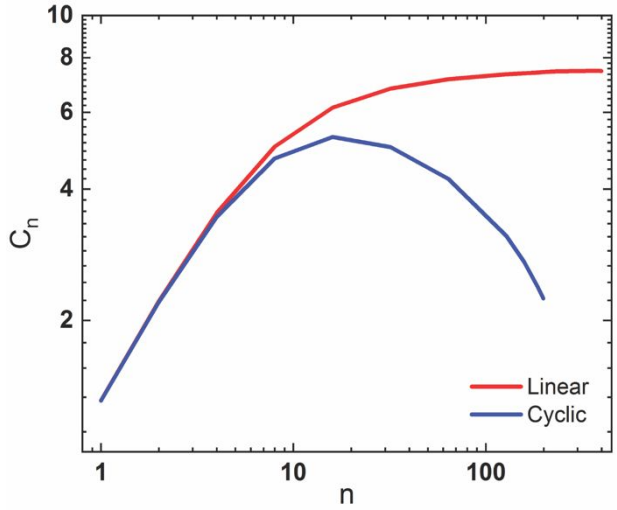

Figure 8. $C(n)$ as a function of n for the linear and cyclic PE melt samples equilibrated at $T_0 = 500K$.

The PE melt samples were crosslinked with one crosslink every 100 CG beads. To simulate crosslinking, the 50th, 150th, 250th, and 350th beads along a polymer chain were designated as crosslinkable beads. One additional harmonic bond formed between two crosslinkable beads when they were separated by less than 1.07 σ and had not been cross-linked yet. At the end of the cross-lining, 97.5% and 98.5% of cross-linkable beads had been linked in the linear and cyclic polymer samples, respectively. The crosslinked samples were cooled to $T = 0.6\ T_0 =\ 300\ K$ at a cooling rate of $5.4\times10^{-5}T_0/\tau$=10 K/ns . During the cooling process, the temperature was controlled

using the Nosé-Hoover thermostat with characteristic damping time 2 τ. Meanwhile, the sample volume was allowed to change under constant pressure $P = 8.0k_BT_0/\sigma^3$, which was controlled using the Nosé-Hoover barostat with characteristic damping time 100 τ.

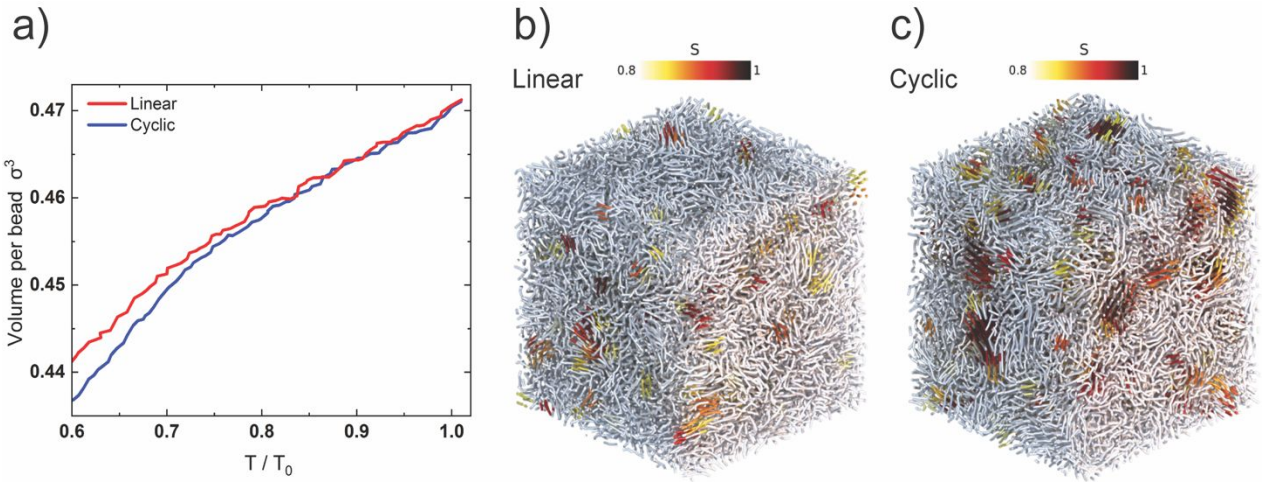

Figure 9. (a) Specific volume vs. temperature for the cooling of the crosslinked linear and cyclic PE samples from $T_0 = 500\,K$ to $0.6\,T_0 = 300\,K$. Snapshots of the samples at the end of the cooling are shown in (b) and (c) with crystalline domains colored based on the order parameter S.

Figure 9a shows the specific volume per CG bead as a function of temperature. Changes in the slope of the decrease of specific volume with decreasing T indicate the changes in the thermodynamic state of the sample due to the emergence of crystalline domains. To identify the crystalline domains, the simulation box is divided into cubic cells of side length 2 σ. For each cell, the nematic tensor $Q_{\alpha\beta} = \sum_{i=1}^{N_{bond}}\left(3/2b_\alpha^i b_\beta^i - 1/2\delta_{\alpha\beta}\right)$ is computed, where α and $\beta \in \{x,y,z\}$, and b_α^i or b_β^i is a component of the unit bond vector for the i-th bond out of the N_{bond} bonds in the cell. The largest eigenvalue of $Q_{\alpha\beta}$ is identified as the order parameter S. The volume fraction of cells with $S > 0.8$ is defined as the degree of crystallinity X_C.[47, 48] At the end of the cooling, $X_C = 6.1\%$ and 13.5% was obtained for the crosslinked linear and cyclic PE samples, respectively. The semi-crystalline morphology of the two samples is visualized in **Figures 9b-c**, where the crystalline domains with $S > 0.8$ are colored based on the value of S. Previous simulations have demonstrated the effects of cooling rate on crystallinity.[44] The cooling rate here was selected to allow X_C at the end of the cooling to be low, as in the experiments of crosslinked PCOE. The results in **Figure 9** also show the change from the linear topology to the non-concatenated cyclic

topology increases X_C, which presumably is related to the faster dynamics of non-concatenated cyclic polymers with fewer entanglements.[39, 41] This result is somehow different from the experimental observation. The detailed effects of non-concatenated cyclic topology on polymer crystallization would be an interesting topic for future study.

The mechanical properties of the crosslinked semi-crystalline PE samples were measured by the uniaxial tensile test. The size of the simulation box in the z-direction expanded at a constant true strain rate of $10^{-4}\,\tau^{-1}$. The rate enabled the tensile test to be conducted within a feasible simulation time yet not so high to cause strong rate-dependent effects. The dimensions of the simulation box in the x- and y-directions varied under constant pressure $P_x = P_y = 8.0\,k_BT/\sigma^3$. The pressure was controlled by the Nosé-Hoover barostat with characteristic damping time $100\,\tau$. During the tensile deformation, the temperature was maintained at $T = 0.6\,T_0$ using the Nosé-Hoover thermostat with characteristic damping time $2\,\tau$.

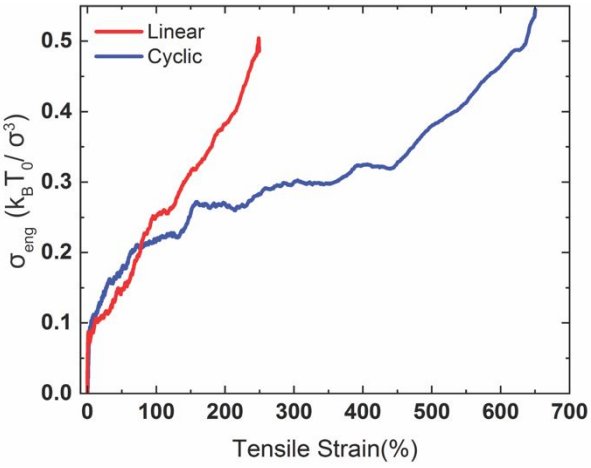

Figure 10. Engineering tensile stress vs. the tensile strain for the crosslinked linear and cyclic PE samples. The tensile tests were simulated at $T = 0.6\,T_0 = 300\,K$ with a deformation rate of $10^{-4}\,\tau^{-1}$.

Figure 10 shows the engineering tensile stress as a function of the stretch ratio $\varepsilon = \lambda - 1$, where λ is the ratio of the box size in the z-direction over its original value in the undeformed state. Since the harmonic bonds cannot capture well the bond extension and breaking behavior, the stress-stretch curve is terminated at ε_{max}, where the distribution of bond length in the undeformed state begins to be biased due to bond extension. $\varepsilon_{max} = 250\%$ and 650% for the crosslinked linear and cyclic PE samples, respectively. The stress-stretch curves for both samples share the same

general features, including the initial elastic response, subsequent yielding, and strain hardening. The two samples have almost the same elastic response and yielding behaviors, as their degrees of crystallinity are comparable. The two samples differ more remarkably in the strain hardening regime. Compared to the linear PE sample, the cyclic PE sample is more stretchable with a larger ε_{max} and exhibits reduced stress at large strain. This trend agrees with the experiment result that the crosslinked cyclic PCOE samples are more stretchable and softer than the corresponding linear samples.

Conformation changes of individual network strands underlie the mechanical response of a crosslinked polymer network. The conformations of network strands, each consisting of 100 CG bonds between two neighboring crosslinks along the polymer contour, are quantified by the root-mean-square end-to-end size in the three orthogonal directions $\langle d_i^2 \rangle^{1/2}$, where $i = x$, y, or z. **Figure 11a** shows $\langle d_i^2 \rangle$ as a function of ε for both crosslinked samples. $\langle d_z^2(\varepsilon) \rangle^{1/2}$ increases while $\langle d_x^2(\varepsilon) \rangle^{1/2}$ and $\left\langle d_y^2(\varepsilon) \right\rangle^{1/2}$ decrease with increasing ε, indicating the network strands are oriented along the stretching direction and pulled taut as well. The predictions of the affine deformation model,[49] where the system volume is conserved upon stretching, are $\langle d_z^2(\varepsilon) \rangle^{1/2} = \lambda \langle d_z^2(\varepsilon = 0) \rangle^{1/2}$, $\langle d_x^2(\varepsilon) \rangle^{1/2} = \lambda^{-1/2} \langle d_x^2(\varepsilon = 0) \rangle^{1/2}$, and $\left\langle d_y^2(\varepsilon) \right\rangle^{1/2} = \lambda^{-1/2} \left\langle d_y^2(\varepsilon = 0) \right\rangle^{1/2}$. These predictions are indicated by the dashed lines for the z-component and the dotted lines for the x- or y-component in **Figure 11a**. The affine deformation model predicts network strand conformations well in crosslinked linear polymers. The network strand stretchability at the end of the stretching is $\varepsilon_{max} = 220\%$, close to the prediction of 250% by the model. However, the affine deformation model overpredicts the changes in network strand conformations in cross-linked cyclic polymers. The network strand stretchability at the end of the stretching is $\varepsilon_{max} = 500\%$, below the prediction of 650% by the model.

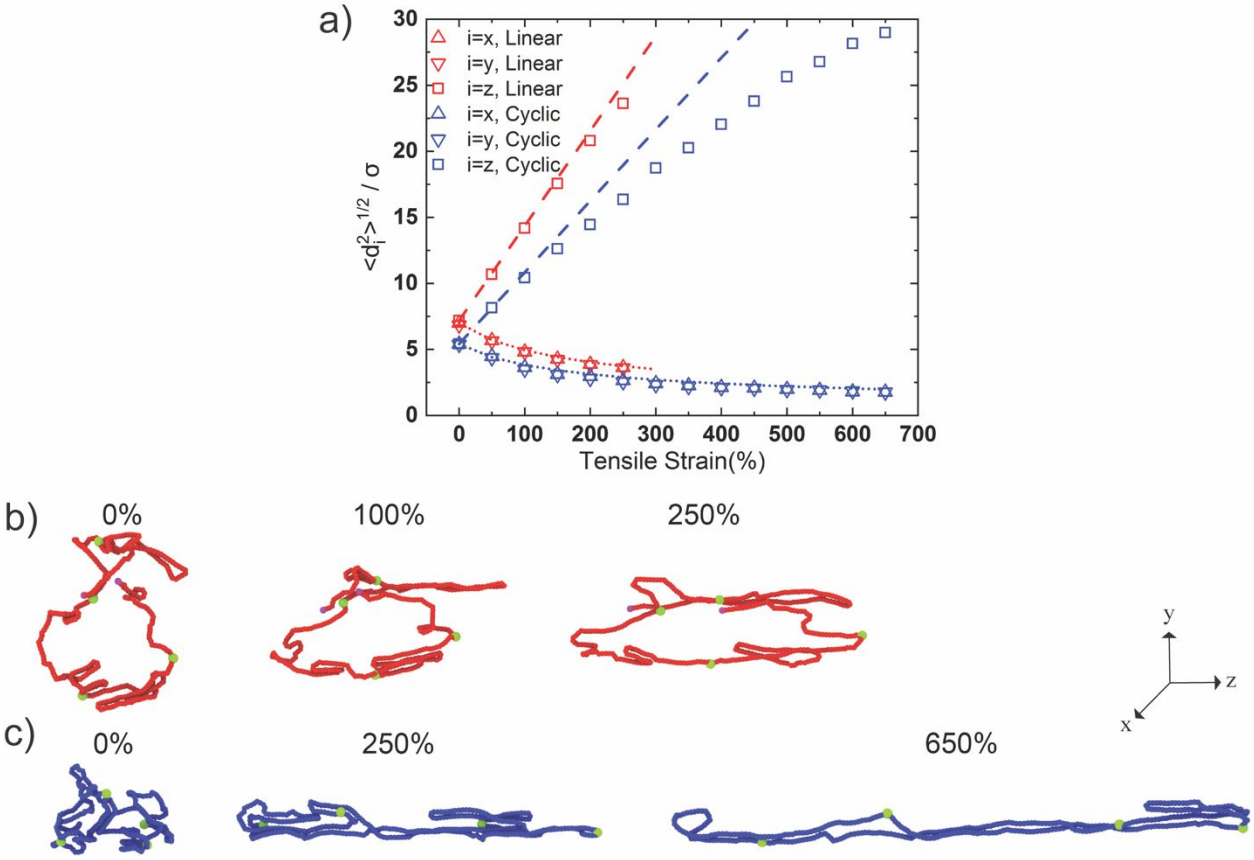

Figure 11. (a) The three components of the root-mean-square end-to-end size of a network strand for the crosslinked linear (red symbols) and cyclic (blue symbols) PE samples as functions of ε. The dashed lines and dotted lines indicate the predictions of the affine deformation model for the components along and normal to the stretching direction, respectively. (b) and (c) visualize the evolutions of a selected linear polymer and a selected cyclic polymer upon stretching. Green spheres indicate crosslinks, and magenta spheres indicate the two ends of the linear chain.

The larger stretchability of network strands and more deviation from the affine deformation in crosslinked cyclic polymers arise from fewer entanglements between the network strands. As visualized in **Figures 11b-c**, a cyclic polymer is more compact than a linear polymer before the deformation (see **Figure 8** for the quantitative characterization). As a result, the mutual overlap of cyclic polymers and the formation of entanglements between them are reduced with respect to the linear polymers. Upon stretching, there are fewer entanglements to prevent the unfolding of the contour length of a network strand. Therefore, a network strand of crosslinked cyclic polymers is less tortuous than that of crosslinked linear polymers at the end of the stretching, as compared in

Figures 11b-c. The lack of sufficient entanglements between crosslinks also leads to the deviation from the affine deformation. With fewer entanglements, the stress level in crosslinked cyclic polymers decreases compared to that in crosslinked linear chains at the same ε.

Conclusions

In summary, this study investigates the mechanical properties of semicrystalline cyclic PCOE synthesized through REMP and linear PCOE synthesized via ROMP, highlighting differences in their crosslinked structures. Crosslinked cyclic PCOE is softer and more stretchable than its linear counterpart due to a lower rubbery modulus and tensile strength, along with fewer entanglements, which enhance polymer mobility and response. Both forms are semicrystalline, with cyclic PCOE showing slightly reduced crystallinity compared to linear PCOE. Molecular dynamics simulations of a similar polymer, PE, support these findings, showing lower stress levels and greater network stretchability in cyclic polymers due to compact conformations and lack of entanglements. These insights align with prior studies on amorphous glassy and elastomeric cyclic polymers, expanding understanding of cyclic polymer mechanics. This research underscores the potential for tailoring cyclic polymers' properties by modifying chain architecture and suggests future studies on blends of cyclic and linear polymers, as well as cyclic polymers with varied crystallinity levels, to further explore the impact of crystallinity on mechanical behavior.

Supplementary Information

Electronic supplementary information (ESI) available. See DOI: https://doi.org/10.1039/.

^{1}H and ^{13}C NMR spectra of compounds, catalysts, and polymers; pictures of crosslinked processes and films; DSC and TGA plots of polymers.

Notes: The authors declare no competing financial interest.

Acknowledgments

We thank Dr. Tianyu Li from Tosoh Bioscience, LLC, for some of the molecular weight analysis. C. T. acknowledges the support from the National Science Foundation award DMR1806792. C. S. S. and M. S. acknowledge support by the NSF CAREER program, NSF award No. DMR-

1752615. T. G. acknowledges start-up funds from the University of South Carolina and the National Science Foundation CAREER award DMR-2236693. Computational resources were provided by University of South Carolina flagship computing cluster Hyperion.

References

1. P. J. Stals, Y. Li, J. Burdynska, R. Nicolaÿ, A. Nese, A. R. Palmans, E. Meijer, K. Matyjaszewski and S. S. Sheiko, *J. Am. Chem. Soc.*, 2013, **135**, 11421-11424.
2. S. J. Garcia, *Eur. Polym. J.*, 2014, **53**, 118-125.
3. B. D. Edgecombe, J. A. Stein, J. M. Fréchet, Z. Xu and E. J. Kramer, *Macromolecules*, 1998, **31**, 1292-1304.
4. J. L. Self, A. J. Zervoudakis, X. Peng, W. R. Lenart, C. W. Macosko and C. J. Ellison, *JACS Au*, 2022, **2**, 310-321.
5. R. Pires-Oliveira, J. Tang, A. M. Percebom, C. L. Petzhold, K. C. Tam and W. Loh, *Langmuir*, 2020, **36**, 15018-15029.
6. J. Yang, R. Bai, B. Chen and Z. Suo, *Adv. Funct. Mater.*, 2020, **30**, 1901693.
7. J. R. Dorgan, H. Lehermeier and M. Mang, *J. Polym. Environ.*, 2000, **8**, 1-9.
8. P. Spitael and C. W. Macosko, *Polym. Eng. Sci.*, 2004, **44**, 2090-2100.
9. K. B. Buhl, A. H. Agergaard, M. Lillethorup, J. P. Nikolajsen, S. U. Pedersen and K. Daasbjerg, *Polymers*, 2020, **12**, 1475.
10. S. Honda, T. Yamamoto and Y. Tezuka, *J. Am. Chem. Soc.*, 2010, **132**, 10251-10253.
11. N. Zaldua, R. Liénard, T. Josse, M. Zubitur, A. Mugica, A. Iturrospe, A. Arbe, J. De Winter, O. Coulembier and A. J. Müller, *Macromolecules*, 2018, **51**, 1718-1732.
12. Y. Lin, Y. Zhang, Z. Wang and S. L. Craig, *J. Am. Chem. Soc.*, 2019, **141**, 10943-10947.
13. K. Zhang, M. A. Lackey, J. Cui and G. N. Tew, *J. Am. Chem. Soc.*, 2011, **133**, 4140-4148.
14. G. S. Grest, T. Ge, S. J. Plimpton, M. Rubinstein and T. C. O'Connor, *ACS Polymers Au*, 2023, **3**, 209-216.
15. J. Wang, T. C. O'Connor, G. S. Grest and T. Ge, *Phys. Rev. Lett.*, 2022, **128**, 237801.
16. H. R. Kricheldorf, *J. Polym. Sci., Part A: Polym. Chem.*, 2010, **48**, 251-284.
17. M. E. Córdova, A. T. Lorenzo, A. J. Müller, J. N. Hoskins and S. M. Grayson, *Macromolecules*, 2011, **44**, 1742-1746.
18. R. Pasquino, T. C. Vasilakopoulos, Y. C. Jeong, H. Lee, S. Rogers, G. Sakellariou, J. Allgaier, A. Takano, A. R. Brás, T. Chang, S. Gooßen, W. Pyckhout-Hintzen, A. Wischnewski, N. Hadjichristidis, D. Richter, M. Rubinstein and D. Vlassopoulos, *ACS Macro Lett.*, 2013, **2**, 874-878.
19. J. Wang and T. Ge, *Macromolecules*, 2021, **54**, 7500-7511.
20. A. Wijesekera, D. L. Vigil and T. Ge, *Macromolecules*, 2024, **57**, 5092-5104.
21. A. Wijesekera, D. L. Vigil, G. S. Grest, S. Zhang and T. Ge, *ACS Macro Lett.*, 2024, DOI: 10.1021/acsmacrolett.4c00446, 1311-1317.
22. F. M. Haque and S. M. Grayson, *Nat. Chem.*, 2020, **12**, 433-444.
23. L. Zhang, Y. Wu, S. Li, Y. Zhang and K. Zhang, *Macromolecules*, 2020, **53**, 8621-8630.
24. L. Qu, P. Sun, Y. Wu, K. Zhang and Z. Liu, *Macromol. Rapid Commun.*, 2017, **38**, 1700121.

25. T. Josse, J. De Winter, P. Gerbaux and O. Coulembier, *Angew. Chem. Int. Ed.*, 2016, **55**, 13944-13958.
26. P. Sun, J. Chen, J. a. Liu and K. Zhang, *Macromolecules*, 2017, **50**, 1463-1472.
27. W. Liu, S. Zhang, S. Liu, Z. Wu and H. Chen, *Macromol. Rapid Commun.*, 2019, **40**, 1900310.
28. D. E. Lonsdale, C. A. Bell and M. J. Monteiro, *Macromolecules*, 2010, **43**, 3331-3339.
29. D. M. Eugene and S. M. Grayson, *Macromolecules*, 2008, **41**, 5082-5084.
30. D. Lu, Z. Jia and M. J. Monteiro, *Polym. Chem.*, 2013, **4**, 2080-2089.
31. S. Sharma, K. Ntetsikas, V. Ladelta, S. Bhaumik and N. Hadjichristidis, *Polym. Chem.*, 2021, **12**, 6616-6625.
32. H. R. Kricheldorf, M. Al-Masri and G. Schwarz, *Macromolecules*, 2002, **35**, 8936-8942.
33. H. R. Kricheldorf and S.-R. Lee, *Macromolecules*, 1996, **29**, 8689-8695.
34. W. Jeong, J. L. Hedrick and R. M. Waymouth, *J. Am. Chem. Soc.*, 2007, **129**, 8414-8415.
35. P. T. Boeck, R. Yadav, B. S. Sumerlin and A. S. Veige, *Macromolecules*, 2024, **57**, 71-77.
36. C. W. Bielawski, D. Benitez and R. H. Grubbs, *Science*, 2002, **297**, 2041-2044.
37. A. J. Boydston, T. W. Holcombe, D. A. Unruh, J. M. J. Fréchet and R. H. Grubbs, *J. Am. Chem. Soc.*, 2009, **131**, 5388-5389.
38. Y. Xia, A. J. Boydston, Y. Yao, J. A. Kornfield, I. A. Gorodetskaya, H. W. Spiess and R. H. Grubbs, *J. Am. Chem. Soc.*, 2009, **131**, 2670-2677.
39. T. Ge, S. Panyukov and M. Rubinstein, *Macromolecules*, 2016, **49**, 708-722.
40. M. Kruteva, J. r. Allgaier, M. Monkenbusch, L. Porcar and D. Richter, *ACS Macro Lett.*, 2020, **9**, 507-511.
41. M. Kapnistos, M. Lang, D. Vlassopoulos, W. Pyckhout-Hintzen, D. Richter, D. Cho, T. Chang and M. Rubinstein, *Nat. Mater.*, 2008, **7**, 997-1002.
42. Z. Lingyi and Z. Wenlin, *Macromolecules*, 2022, **55**, 4899-4906.
43. E. Törnquist, L. Gentile, S. Prévost, A. Diaz, U. Olsson and H. Isaksson, *Sci. Rep.*, 2020, **10**, 14552.
44. W. S. Fall, J. Baschnagel, O. Lhost and H. Meyer, *Macromolecules*, 2022, **55**, 8438-8450.
45. A. P. Thompson, H. M. Aktulga, R. Berger, D. S. Bolintineanu, W. M. Brown, P. S. Crozier, P. J. In't Veld, A. Kohlmeyer, S. G. Moore and T. D. Nguyen, *Comput. Phys. Commun.*, 2022, **271**, 108171.
46. T. P. Lodge and P. C. Hiemenz, *Polymer chemistry*, CRC press, 2020.
47. S. Jabbari-Farouji, J. Rottler, O. Lame, A. Makke, M. Perez and J.-L. Barrat, *J. Phys.: Condens. Matter*, 2015, **27**, 194131.
48. S. Jabbari-Farouji, O. Lame, M. Perez, J. Rottler and J.-L. Barrat, *Phys. Rev. Lett.*, 2017, **118**, 217802.
49. M. Rubinstein and R. H. Colby, *Polymer physics*, Oxford university press, 2003.

Data Availability Statement:

The datasets supporting this article have been uploaded as part of the supplementary information.